

# Strain-Regulated Pd/Cu Core/Shell Icosahedra for Tunable Syngas Electrosynthesis from CO<sub>2</sub>

Hanjun Li, Nan Zhang,\* Shuxing Bai, Longsheng Zhang, Feili Lai, Yao Chen, Xiangmiao Zhu, and Tianxi Liu\*



Cite This: *Chem. Mater.* 2022, 34, 7995–8003



Read Online

ACCESS |



Metrics & More

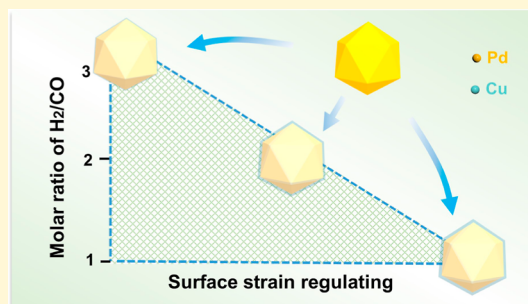


Article Recommendations



Supporting Information

**ABSTRACT:** Introducing surface strain into catalysts would optimize the adsorption energy and surface electronic structure, but it is rarely used in the carbon dioxide reduction reaction (CO<sub>2</sub>RR) to regulate syngas. Herein, we have demonstrated a new class of Pd/Cu core/shell icosahedra (ico) with a tensile-strained Cu shell for efficient syngas production with tunable compositions from the CO<sub>2</sub>RR for the first time. By tuning the composition of Pd/Cu from 2.2 to 4.3 and 6.1, the molar ratio of H<sub>2</sub>/CO in syngas on Pd/Cu core/shell ico could be tuned from 1/1 to 2/1 and 3/1, respectively. The variable selectivity of the CO<sub>2</sub>RR on Pd/Cu core/shell ico originated from the tensile-strained Cu shell, which synergistically optimizes the binding energy of the intermediate and the electronic structure of catalysts. The work reveals how surface strain regulation accelerates electrocatalytic performance at the molecular level, providing new strategies to regulate CO<sub>2</sub>RR performance.



## INTRODUCTION

Using CO<sub>2</sub> as a potential carbon source to obtain high-value chemical products through electrochemical catalysis is an ideal strategy of CO<sub>2</sub> conversion, which can directly convert CO<sub>2</sub> into diverse energy materials, thus closing the man-made carbon cycle.<sup>1–4</sup> At present, most of the research on the CO<sub>2</sub> reduction reaction (CO<sub>2</sub>RR) is mainly to pursue high Faradaic efficiency (FE) and yield of products such as methane, methanol, formate, and multi-carbon products.<sup>5–7</sup> Therefore, it is significant to develop high-performance electrocatalysts for the CO<sub>2</sub>RR and suppress the side reaction of the hydrogen evolution reaction (HER), which is generally performed under cathodic conditions in an aqueous electrolyte.<sup>8,9</sup> Although significant efforts have been made to prohibit the HER by designing electrocatalysts, the low selectivity of the CO<sub>2</sub>RR remains a key challenge.

In addition to inhibiting the HER, making full use of the products of the HER and CO<sub>2</sub>RR, combining these two products to obtain syngas (H<sub>2</sub> and CO) is an alternative and effective method to convert CO<sub>2</sub>.<sup>10–12</sup> The produced syngas with a tunable composition is readily used to produce valuable chemicals for the Fischer–Tropsch, methanol synthesis reactions and so on.<sup>13–15</sup> With regard to these thermochemical processes, the product selectivity is mainly determined by the molar ratio of H<sub>2</sub>/CO.<sup>16–18</sup> Therefore, controlling the composition of syngas will provide universality for the use of H<sub>2</sub> and CO in electrocatalytic methods. However, achieving high CO<sub>2</sub>RR activity while maintaining a tunable composition of syngas within the ideal range during the thermochemical process is not an easy task.

As we all know, palladium (Pd) has superior catalytic activity for the HER, but it was considered to be unsuitable for CO production during the CO<sub>2</sub>RR due to its strong CO binding.<sup>19–21</sup> Icosahedra (ico), a kind of multiple-twinned nanoparticles, have demonstrated excellent catalytic performance in many different reactions.<sup>22</sup> In addition, modifying the catalyst surface with foreign metals can provide more possibilities for regulating the activity and selectivity of the CO<sub>2</sub>RR,<sup>23–25</sup> which is attributed to the fact that the strain effects introduced by the metal shell optimizes the binding energy of the intermediates in the CO<sub>2</sub>RR.<sup>26,27</sup> Above all, introducing the metal overlayers onto the Pd ico would optimize the strain effect of the catalyst, which has the potential to control the types of products in the CO<sub>2</sub>RR. However, introducing a metal layer on the strained Pd ico surface has rarely been reported in the CO<sub>2</sub>RR to syngas.

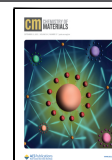
## EXPERIMENTAL SECTION

**Materials.** Palladium(II) acetylacetonate [Pd(acac)<sub>2</sub>, 99%], sodium tetrachloropalladate (Na<sub>2</sub>PdCl<sub>4</sub>, 99.9%), ammonium bromide (NH<sub>4</sub>Br), polyvinyl pyrrolidone [(C<sub>6</sub>H<sub>9</sub>NO)<sub>n</sub>, PVP, molecular weight = 58,000], and copper formate [Cu(COOH)<sub>2</sub>] were obtained from Sigma-Aldrich. Ethanol (C<sub>2</sub>H<sub>6</sub>O, ≥99.7%), *N,N*-dimethylformamide

Received: June 27, 2022

Revised: August 9, 2022

Published: August 19, 2022



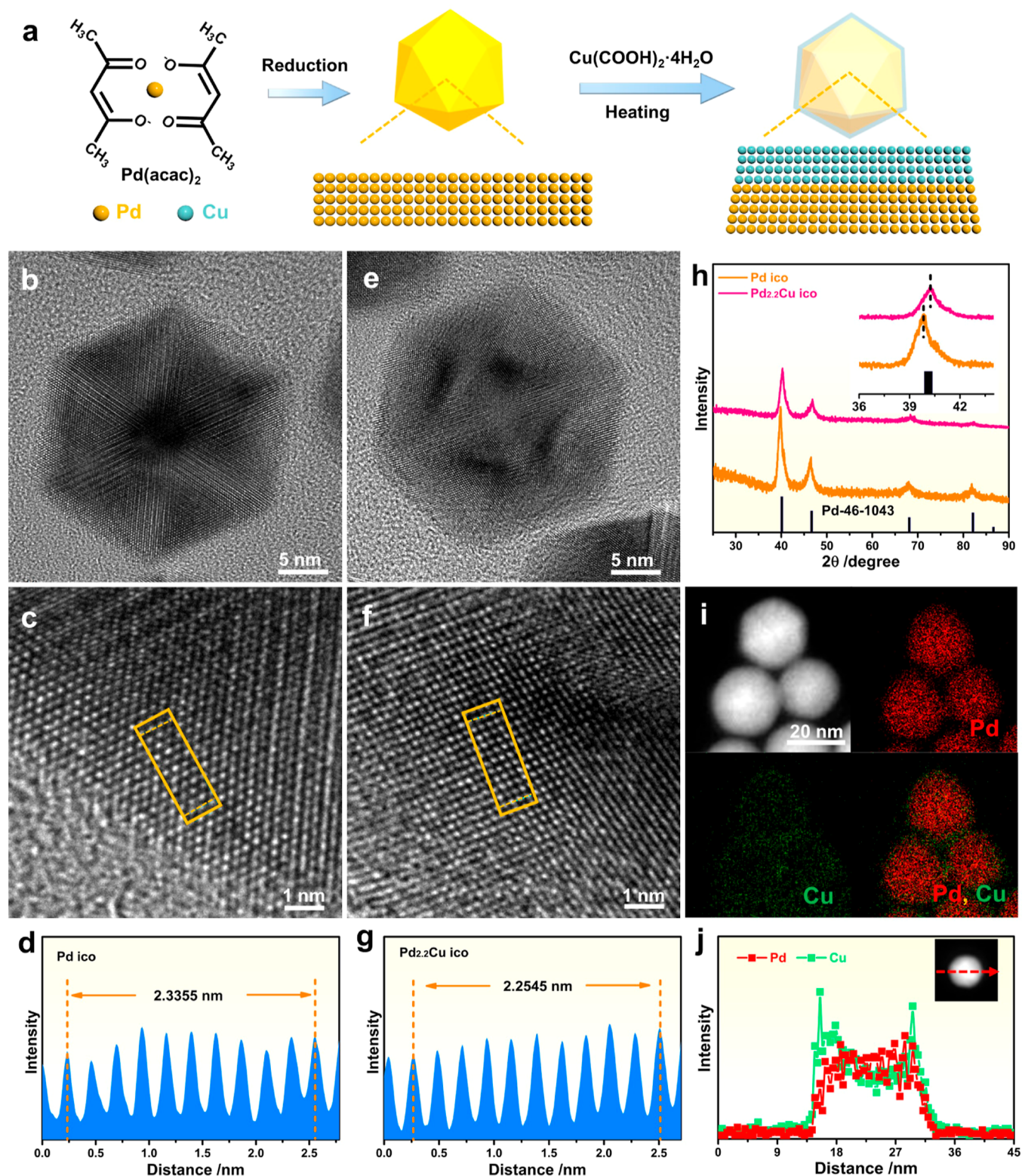


**Figure 1.** Synthesis and structural characterization of Pd<sub>2.2</sub>Cu core/shell ico. (a) Schematic illustration of the synthesis of Pd<sub>2.2</sub>Cu ico. (b,e) TEM images and (c,f) their corresponding HRTEM images of one typical Pd ico and Pd<sub>2.2</sub>Cu ico. (d,g) Integrated pixel intensities and interplanar spacings of Pd {111} lattices of Pd ico and Pd<sub>2.2</sub>Cu ico. (h) PXRD patterns of Pd ico and Pd<sub>2.2</sub>Cu ico. (i) EDS elemental mappings and (j) line-scan profile across the Pd<sub>2.2</sub>Cu ico marked by the right arrow in the inset.

(C<sub>3</sub>H<sub>7</sub>NO, DMF), acetone (C<sub>3</sub>H<sub>6</sub>O, ≥99.7%), formic acid aqueous solution (HCOOH, ≥85%), sodium iodide (NaI, 99.0%), and ethylene glycol (EG) (C<sub>2</sub>H<sub>6</sub>O<sub>2</sub>, EG, ≥99.0%) were obtained from Sinopharm Chemical Reagent Co. Ltd (Shanghai, China). Molybdenum hexacarbonyl [Mo(CO)<sub>6</sub>, 98%, Strem Chemicals] and ascorbic acid

(C<sub>6</sub>H<sub>8</sub>O<sub>6</sub>, AA, 99%, J&K China Chemical Ltd) were used as received. The water (18 MΩ/cm) used in all electrolyte solutions was obtained using an ultra-pure purification system.

**Preparation of Pd ico.** Pd(acac)<sub>2</sub> (7.4 mg), NH<sub>4</sub>Br (15 mg), and PVP (50 mg) were dissolved in 10 mL of DMF. The mixture was further

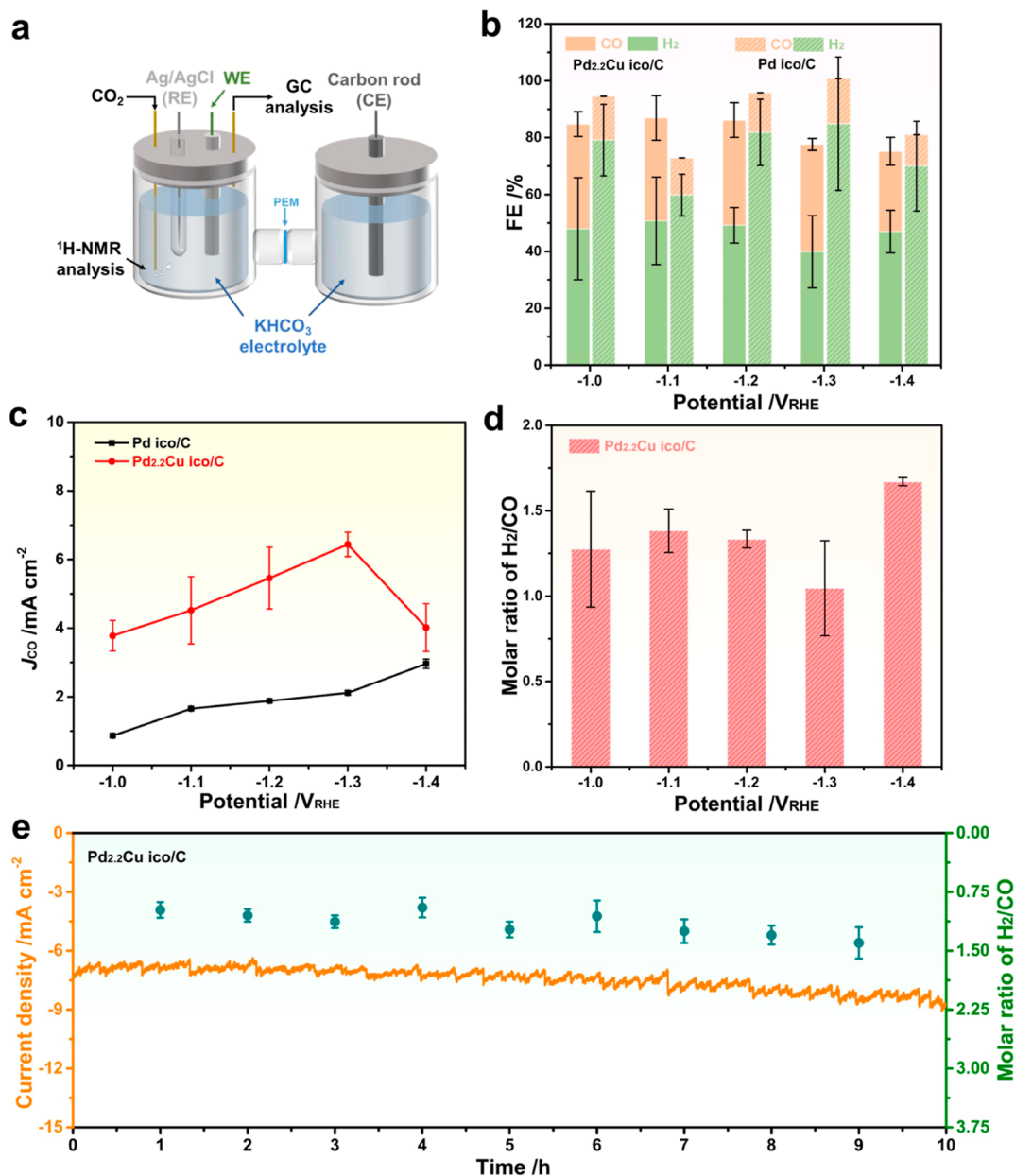


**Figure 2.** CO<sub>2</sub>RR performances of Pd ico/C and Pd<sub>2.2</sub>Cu ico/C. (a) Schematic diagram of the CO<sub>2</sub>RR setup. (b) FEs of main reduction products (H<sub>2</sub> and CO) at varied applied potentials of Pd ico/C and Pd<sub>2.2</sub>Cu ico/C. (c) Potential-dependent CO partial current densities of two different catalysts. (d) Molar ratio of H<sub>2</sub>/CO by Pd<sub>2.2</sub>Cu ico/C at different potentials. (e) Time-dependent current density over Pd<sub>2.2</sub>Cu ico/C at -1.3 V<sub>RHE</sub>.

heated to 180 °C for 2 h in an oil bath to obtain Pd ico, which were collected by centrifugation and washed with ethanol and acetone.

The mixture of Na<sub>2</sub>PdCl<sub>4</sub> (7.4 mg), HCOOH (0.5 mL), PVP (20 mg), NaI (5 mg), and DMF (10 mL) and the mixture of Pd(acac)<sub>2</sub> (7.4 mg), HCOOH (0.1 mL), PVP (100 mg), Mo(CO)<sub>6</sub> (1 mg), and DMF (10 mL) were heated to 120 °C for 5 h in an oil bath to prepare Pd nanocubes and tetrahedra, respectively.

**Preparation of Pd<sub>6.1</sub>Cu ico, Pd<sub>4.3</sub>Cu ico, and Pd<sub>2.2</sub>Cu ico.** As for Pd<sub>6.1</sub>Cu ico, Pd ico (0.5 mg) were dispersed in EG (4 mL) into a vial, then Cu(COOH)<sub>2</sub> (0.6 mg) and AA (18.8 mg) were added into the vial. The mixture was ultrasonicated for around 5 min. The other conditions (reaction temperature and time) of Pd<sub>6.1</sub>Cu ico were the same as those for the Pd ico. The preparation of Pd<sub>4.3</sub>Cu ico and Pd<sub>2.2</sub>Cu ico was similar to that of Pd<sub>6.1</sub>Cu ico except that the amount of Cu(COOH)<sub>2</sub> was increased to 1.2 and 2.4 mg, respectively. The preparation of Pd/Cu core/shell nanocubes and tetrahedra was similar to that of Pd<sub>2.2</sub>Cu ico except for the change of Pd ico.

**Characterizations.** Transmission electron microscopy (TEM) images were collected using a JEM-2100plus transmission electron microscope at 120 kV. High-resolution TEM (HRTEM) and scanning transmission electron microscopy (STEM) images were captured using an FEI Tecnai F20 transmission electron microscope at 200 kV. SEM-energy-dispersive X-ray spectroscopy (EDS) was performed using a HITACHI S-4800 at 30 kV. Powder X-ray diffraction (PXRD) patterns were collected using a Philips X'Pert Pro Super diffractometer with Cu K $\alpha$  radiation ( $\lambda = 0.15406$  nm). X-ray photoelectron spectroscopy (XPS) spectra were obtained using a Kratos AXIS SUPRA<sup>+</sup> spectrometer equipped with a monochromatic Al K $\alpha$  X-ray source operating at 600 W. <sup>1</sup>H nuclear magnetic resonance (<sup>1</sup>H NMR) spectra were obtained using a 400 MHz NMR spectroscope (AVANCE III HD).

**Electrochemical Measurements.** The electrochemical measurements of the CO<sub>2</sub>RR were conducted in a closed H-type electrolytic cell using a CHI 660e separated from the Nafion membrane. The Pd-based ico catalysts were dispersed in a mixture containing isopropanol and

Nafion (5%) to form a 0.50 mg<sub>Pd</sub>/mL dispersion. A 40  $\mu$ L dispersion of Pd ico/C, Pd<sub>6.1</sub>Cu ico/C, Pd<sub>4.3</sub>Cu ico/C, and Pd<sub>2.2</sub>Cu ico/C was deposited on a right angle glassy carbon electrode to obtain the working electrodes (WEs).

As for CO stripping measurements, the three-electrode system was also applied for CO stripping measurements at room temperature. First, the electrode was immersed in CO-saturated 0.1 M HClO<sub>4</sub> for around 15 min. Then, the electrode was quickly moved into a fresh 0.1 M HClO<sub>4</sub> solution. Finally, CO stripping curves were obtained by performing sweep cyclic voltammetry for two cycles at 20 mV s<sup>-1</sup>.

As for the CO<sub>2</sub>RR, the electrolyte is 0.1 M KHCO<sub>3</sub> solution. High-purity CO<sub>2</sub> (20 sccm) (99.99%) was purged into 10 mL of 0.1 M KHCO<sub>3</sub> in the cathode compartment for 15 min. The gaseous products were quantified using a gas chromatography system. The liquid products were characterized and quantified by <sup>1</sup>H NMR.

## RESULTS AND DISCUSSION

Herein, we report the monodisperse Pd/Cu core/shell ico for the first time, which are demonstrated to promote tunable syngas production via the CO<sub>2</sub>RR and feature a tensile-strained Cu overlayer on Pd ico. The composition of Pd/Cu can be easily tuned from 2.2 to 4.3 and 6.1, which is closely related to the performance of syngas electro-synthesis from CO<sub>2</sub>. Particularly, the Pd/Cu core/shell ico with different compositions enable tunable molar ratios of H<sub>2</sub>/CO from 1/1 to 2/1 and 3/1, outperforming most of the reported catalysts for syngas electro-synthesis.<sup>28</sup> The mechanistic discussion suggests that the tensile-strained Cu shell may strengthen the binding of CO<sub>2</sub> and decrease the adsorption of CO, favoring the tunable syngas production.

The fabrication process of Pd/Cu core/shell ico is shown in Figure 1a. First, monodisperse, uniform, and high-yield Pd ico were prepared through a hydrothermal method (Figure S1a). Then, Pd ico were dispersed in EG to mix with Cu(COOH)<sub>2</sub> and ascorbic acid (AA). Cu(COOH)<sub>2</sub> was then reduced and precipitated on Pd ico seeds, resulting in the formation of Pd/Cu core/shell ico.<sup>29</sup> The high-angle annular dark-field scanning transmission electron microscopy (HAADF-STEM) and TEM were first employed to investigate the morphology and structure of Pd/Cu core/shell ico (feed ratio of Pd and Cu = 2.5:1). The Pd/Cu ico are fairly uniform in terms of size without any irregular nanoparticles (Figure S1b). According to the particle size distribution of the Pd/Cu ico and Pd ico (Figure S1c,d), the average size of the Pd/Cu ico is around 23.9 nm, which is slightly larger than that of the Pd ico seeds (23.4 nm), indicating that Cu has been successfully epitaxially grown on the Pd ico seed surface. The molar ratio of Pd and Cu was 2.2/1, as determined by EDS (Figure S2a), so that the sample was defined as Pd<sub>2.2</sub>Cu ico. The molar ratio of Pd/Cu on the Pd<sub>2.2</sub>Cu ico surface was further evaluated to be 54.5/45.5 by XPS, revealing that Cu was mainly distributed on the Pd<sub>2.2</sub>Cu ico surface (Figure S2b,c). As shown in the TEM image of the one typical Pd ico and Pd<sub>2.2</sub>Cu ico (Figure 1b,e), it can be clearly seen that they both have obvious twin boundaries. Furthermore, as both Pd ico and Pd<sub>2.2</sub>Cu ico are enclosed by {111} facets, their lattice spacings of {111} planes were compared by HRTEM. As for Pd ico (Figure 1c,d), the lattice spacing of {111} planes is 0.233 nm, slightly larger than that of the single-crystalline bulk, proving that the tensile strain exists on Pd ico.<sup>30</sup> With regard to Pd<sub>2.2</sub>Cu ico (Figure 1f,g), the measured lattice spacing is 0.225 nm, which is slightly smaller than that of Pd ico, indicating the existence of compressive strain after the induction of the Cu shell on Pd ico.

In order to clarify the difference between the crystal phase structures of Pd ico and Pd<sub>2.2</sub>Cu ico, PXRD was also conducted

(Figure 1h). According to their PXRD patterns, it can be seen that both the samples correspond to face-centered cubic (fcc) Pd, while the Cu shell of Pd<sub>2.2</sub>Cu ico is thin enough to be observed. However, there is a clear difference in the peak positions between the two samples. Particularly, the main diffraction peaks of Pd ico shifted to lower angles compared to the standard card of Pd, while those of Pd<sub>2.2</sub>Cu ico shifted toward higher angles than those for Pd ico, demonstrating the smaller lattice constant of Pd<sub>2.2</sub>Cu ico. Specifically, due to the twin structure, the lattice constant of Pd ico became larger. As for the Pd<sub>2.2</sub>Cu ico, owing to the smaller atomic radius of Cu, the tensile-strained Cu overlayer resulted in a smaller lattice spacing of the Pd core, which is consistent with HRTEM results.<sup>31</sup> In addition, the EDS elemental mappings of Pd<sub>2.2</sub>Cu ico show that Pd is concentrated in the interior of the ico, while Cu is distributed on the surface of Pd (Figure 1i). The line-scan analysis shown in Figure 1j reveals that Cu is mainly outside the Pd core. Taken together, due to the difference in the atomic radius of Pd and Cu, the surface Cu shell is subjected to tensile strain by the larger Pd atoms in the Pd core, while the smaller Cu exerts compressive strain on the inner Pd core. In a word, there is tensile strain in the Cu shell, while compressive strain exists in the Pd core.

Before the electrocatalytic experiments, the two different Pd<sub>2.2</sub>Cu ico and Pd ico were first loaded on commercial carbon (Vulcan XC72R carbon, C) *via* sonication (Figure S3). CO<sub>2</sub>RR performance of Pd-based ico/C was further evaluated for constant-potential electrolysis. As shown in Figure 2a, the catalyst-coated glass carbon electrode was used as the WE, a Ag/AgCl electrode was used as the reference electrode (RE), and a carbon rod was used as the counter electrode (CE). The WE and RE were placed in the cathode compartment, while the CE was in anode compartment. CO<sub>2</sub> was continuously passed through the catholyte (0.1 M KHCO<sub>3</sub>), and the gas production was connected to a gas chromatograph. All potentials were calibrated to the reversible hydrogen electrode (RHE) (Figure S4).

Chrono-amperometry results of Pd ico/C and Pd<sub>2.2</sub>Cu ico/C at different potentials are shown in Figure S5. According to the results of gas chromatography, H<sub>2</sub> and CO are the main products of Pd ico and Pd<sub>2.2</sub>Cu ico/C. The <sup>1</sup>H NMR spectrum of Pd<sub>2.2</sub>Cu ico/C at -1.2 V<sub>RHE</sub> shows that the remaining product is formic acid (Figure S6). In addition, Figure 2b shows FEs of both H<sub>2</sub> and CO under different applied potentials. Compared with Pd ico/C, Pd<sub>2.2</sub>Cu ico/C exhibits more CO yields for all the applied potentials. The partial current densities of CO (*j*<sub>CO</sub>) on Pd ico/C and Pd<sub>2.2</sub>Cu ico/C are shown in Figure 2c. Pd<sub>2.2</sub>Cu ico/C exhibits higher *j*<sub>CO</sub> than Pd ico/C at all applied potentials. The molar ratios of H<sub>2</sub>/CO at different potentials by Pd ico/C and Pd<sub>2.2</sub>Cu ico/C are shown in Figures S7 and 2d. It is obvious that the molar ratio of H<sub>2</sub>/CO at all applied potentials by Pd<sub>2.2</sub>Cu ico/C is between 1.0 and 2.0. Particularly, at both -1.2 and -1.3 V<sub>RHE</sub>, the molar ratio of H<sub>2</sub>/CO by Pd<sub>2.2</sub>Cu ico/C is around 1.0, which would be readily used in the hydroformylation process. In sharp contrast to these results, the molar ratios of H<sub>2</sub>/CO by Pd ico/C at all applied potentials are all greater than 4.0, which does not meet the ratio of syngas. Finally, the long-term stabilities of Pd<sub>2.2</sub>Cu ico/C were also investigated using chronoamperometry at -1.3 V<sub>RHE</sub>. As shown in Figure 2e, the current density change of Pd<sub>2.2</sub>Cu ico/C is not significant, and the molar ratios of H<sub>2</sub>/CO are maintained at around 1.0 during the 10 h stability test. Furthermore, the structure, composition, and surface tensile strain of Pd<sub>2.2</sub>Cu ico/C could largely be maintained after the durability test (Figure S8). In addition, Pd 3d and Cu 2p spectra

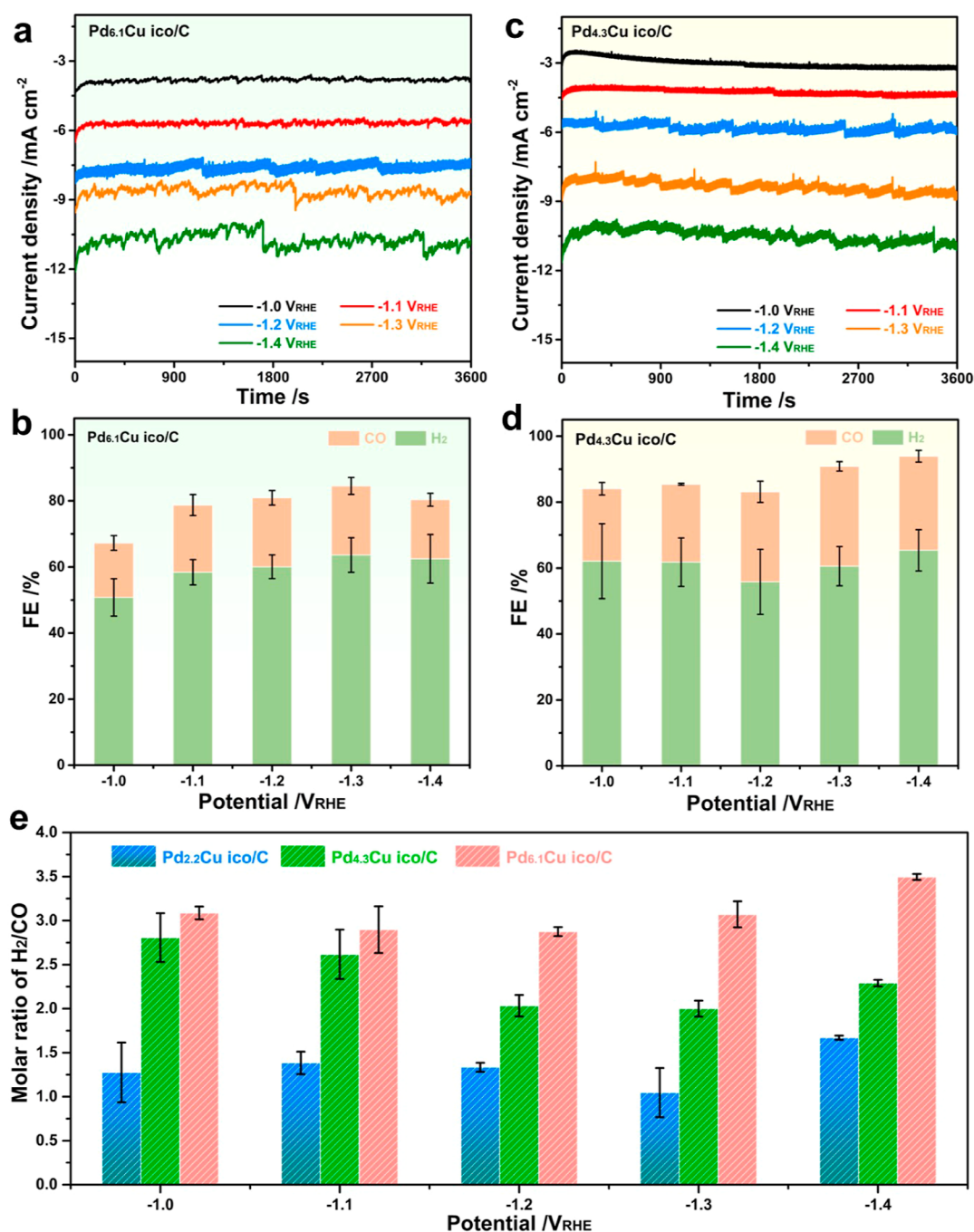


**Figure 3.** CO<sub>2</sub>RR performance of Pd<sub>6.1</sub>Cu ico/C and Pd<sub>4.3</sub>Cu ico/C. (a,c) Chrono-amperometry results, (b,d) FEs of H<sub>2</sub> and CO by Pd<sub>6.1</sub>Cu ico/C and Pd<sub>4.3</sub>Cu ico/C. (e) Molar ratio of H<sub>2</sub>/CO by Pd<sub>2.2</sub>Cu ico/C, Pd<sub>4.3</sub>Cu ico/C, and Pd<sub>6.1</sub>Cu ico/C at applied potentials.

of Pd<sub>2.2</sub>Cu ico/C show that the two elements exist stably after the durability test (Figure S9). Therefore, Pd<sub>2.2</sub>Cu ico would serve as promising catalysts for persistently producing syngas during the CO<sub>2</sub> reduction process.

Encouraged by these results, the monodisperse Pd<sub>6.1</sub>Cu ico and Pd<sub>4.3</sub>Cu ico were obtained by decreasing the Cu content with other synthesis conditions kept the same as those for Pd<sub>2.2</sub>Cu ico (Figure S10a,b) and the average particle sizes of the ico products of about 23.5 and 23.8 nm, respectively (Figure S10c,d). In addition, their atomic ratios were revealed by SEM-EDS, as shown in Figure S10e,f. PXRD peaks of Pd<sub>6.1</sub>Cu ico and Pd<sub>4.3</sub>Cu ico are slightly shifted to a higher angle compared to that of Pd ico (Figure S11), indicating that the strain intensity

can be optimized by changing the amount of Cu. If the amount of Cu(COOH)<sub>2</sub> was further increased to 3.6 mg [Pd(acac)<sub>2</sub>/Cu(COOH)<sub>2</sub> = 1.5], the product is mainly composed of irregular particles (Figure S12a). In addition, the PXRD pattern shows two phases: Pd and Cu (Figure S12b). The results mentioned above reveal that if the amount of Cu is further increased, the Pd/Cu core/shell structure cannot be obtained.

The CO<sub>2</sub>RR performances of the two catalysts with different strain intensities were further studied in the same condition as that for Pd<sub>2.2</sub>Cu ico/C. The Pd<sub>6.1</sub>Cu ico and Pd<sub>4.3</sub>Cu ico were loaded evenly on the carbon support (Figure S13). The chrono-amperometry results for Pd<sub>6.1</sub>Cu ico/C and Pd<sub>4.3</sub>Cu ico/C at different potentials are shown in Figure 3a,c. The FEs of H<sub>2</sub> and

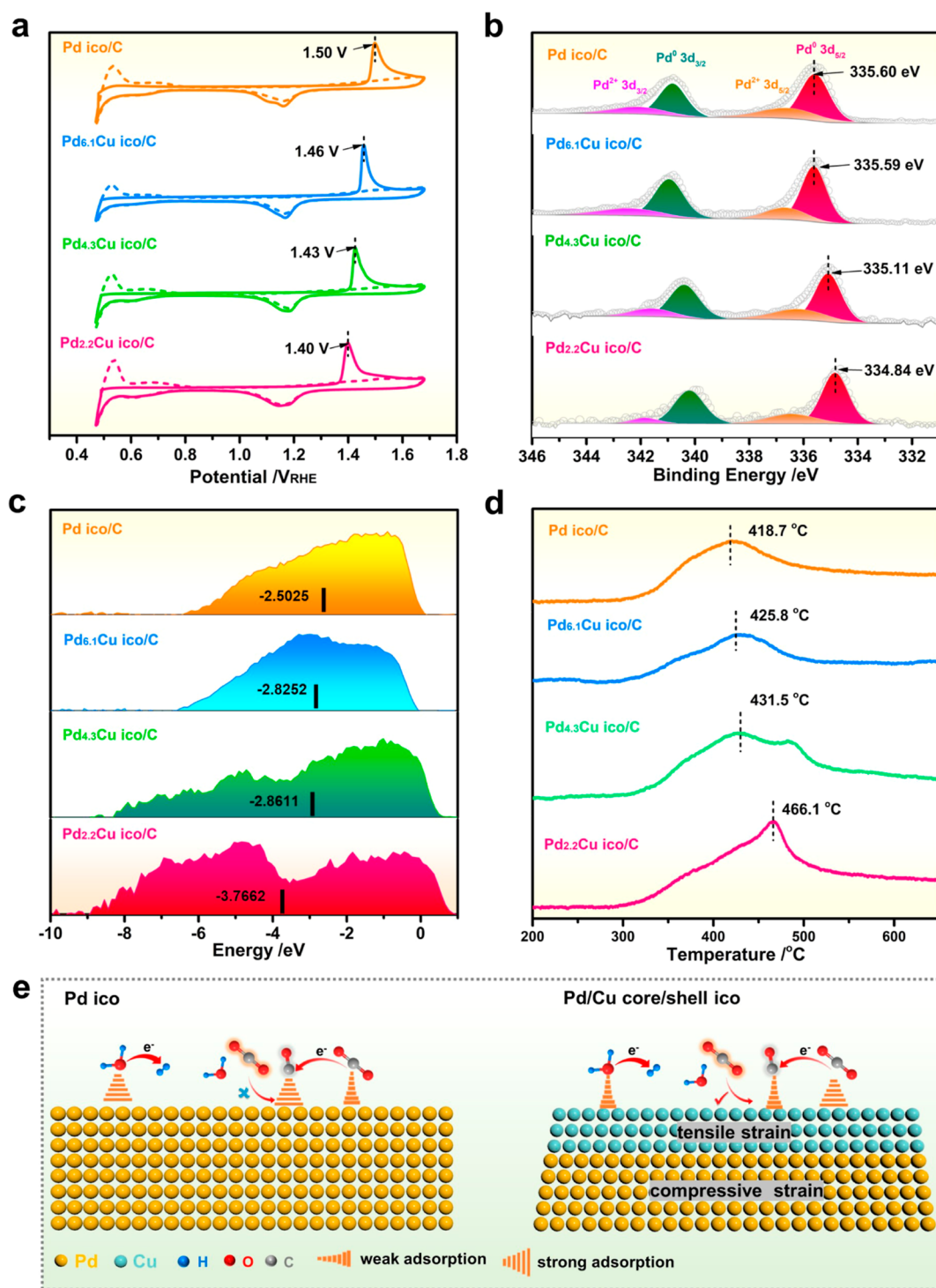


**Figure 4.** (a) CO stripping curves, (b) Pd 3d spectra, (c) valence band spectra, and (d) CO<sub>2</sub>-TPD profiles for Pd ico/C and three different Pd/Cu core/shell ico/C catalysts. (e) Illustrations of the adsorption of reactants and products on Pd ico and Pd/Cu core/shell ico during the electrochemical CO<sub>2</sub>RR.

CO at corresponding potentials for Pd<sub>6.1</sub>Cu ico/C and Pd<sub>4.3</sub>Cu ico/C are shown in Figure 3b,d. It is pertinent that the main products in the CO<sub>2</sub>RR by the two different catalysts are CO and H<sub>2</sub> at all applied potentials. Moreover, the introduction of Cu enhances the FE<sub>CO</sub> of Pd ico in the CO<sub>2</sub>RR, and FE<sub>CO</sub> increases with the increase of the Cu content. As shown in Figure 3e, Pd<sub>6.1</sub>Cu ico/C and Pd<sub>4.3</sub>Cu ico/C can be implemented such that the molar ratio of H<sub>2</sub>/CO in syngas ranges around 3:1 to 2:1. Especially, the developed Pd/Cu ico electrocatalysts enable a

tunable molar ratio of H<sub>2</sub>/CO, ranging from 1/1 to 2/1 and 3/1 at both -1.2 and -1.3 V<sub>RHE</sub> for Pd<sub>2.2</sub>Cu ico/C, Pd<sub>4.3</sub>Cu ico/C, and Pd<sub>6.1</sub>Cu ico/C, respectively. Beyond that, in order to illustrate the important role of Pd ico seeds with a twin structure on the syngas production, Pd/Cu core/shell nanocubes and tetrahedra were prepared by using Pd nanocubes and tetrahedra as seeds, respectively (Figures S14 and S15). Compared with that for Pd/Cu ico/C, the yield of H<sub>2</sub> is much higher than the yield of CO by the two different catalysts during the CO<sub>2</sub>RR

(Figures S16 and S17), far from the proportion of syngas, further highlighting the key role of twinned Pd ico in regulating the adsorption energy of the intermediate.

To further investigate the tolerance ability of \*CO intermediates during the CO<sub>2</sub>RR after the induction of Cu, CO stripping experiments of the four different ico/C catalysts were carried out. As shown in Figure 4a, the position of the \*CO oxidation peaks of Pd<sub>2.2</sub>Cu ico/C is 1.40 V<sub>RHE</sub>, which is lower than those of Pd<sub>4.3</sub>Cu ico/C (1.43 V<sub>RHE</sub>), Pd<sub>6.1</sub>Cu ico/C (1.46 V<sub>RHE</sub>), and Pd ico/C (1.50 V<sub>RHE</sub>), revealing that the induction of Cu would weaken the adsorption energy of \*CO.<sup>32</sup> Moreover, XPS was also conducted to decode their electronic structures (Figures 4b, S2b,c, and S18). Figure 4b shows the Pd 3d spectra of the four different catalysts. As we can see, Pd 3d<sub>3/2</sub> binding energies of the different catalysts decrease gradually with the increase of the Cu content, indicating that electron transfer occurred between Pd and Cu.<sup>33,34</sup> Therefore, the Cu shell of the Pd/Cu core/shell ico could improve the tolerance ability of \*CO intermediates, thereby accelerating the CO<sub>2</sub> reduction kinetics. In addition, as shown in the Nyquist plot (Figure S19), Pd<sub>2.2</sub>Cu ico/C has a smaller charge transfer resistance than Pd ico/C, indicating its faster charge transfer process in CO<sub>2</sub> reduction.

Furthermore, to evaluate the binding strength of intermediates on the Pd/Cu core/shell ico, the d-band center with respect to  $E - E_F$  was measured.<sup>35</sup> Figure 4c shows that the d-band centers of Pd/Cu core/shell ico shift upward with the increasing Cu content, likely enhancing the adsorption of intermediates during the CO<sub>2</sub>RR.<sup>36</sup> In addition, CO<sub>2</sub> temperature-programmed desorption (CO<sub>2</sub>-TPD) was conducted to further study the adsorption of CO<sub>2</sub>. As shown in Figure 4d, the chemical desorption temperature of Pd<sub>2.2</sub>Cu ico/C (466.1 °C) is higher than those of Pd<sub>4.3</sub>Cu ico/C (431.5 °C), Pd<sub>6.1</sub>Cu ico/C (425.8 °C), and Pd ico/C (418.7 °C). It can be clearly observed that the temperature of CO<sub>2</sub> desorption increases with the increase of Cu content, suggesting that the Cu shell on Pd ico remarkably improves the chemisorption ability of CO<sub>2</sub>.<sup>37</sup> Above all, the tensile-strained Cu shell enhances the binding of CO<sub>2</sub> and decreases the adsorption of CO, favoring syngas production with tunable compositions (Figure 4e).

## CONCLUSIONS

In summary, a new class of Pd/Cu core/shell ico for efficient syngas with tunable compositions from the CO<sub>2</sub>RR have been prepared for the first time. With the increase of Cu content in Pd/Cu core/shell ico, the FE<sub>CO</sub> increased. By tuning the composition of Pd/Cu from 2.2 to 4.3 and 6.1, the syngas compositions on Pd/Cu core/shell ico/C are tunable from 1/1 to 2/1 and 3/1, respectively, for H<sub>2</sub>/CO. The mechanistic discussion implies that the tunable syngas production on Pd/Cu core/shell ico/C during the CO<sub>2</sub>RR originated from the tensile-strained Cu shell, which synergistically optimizes the adsorption energy, surface electronic structure, and catalytic performance for the CO<sub>2</sub>RR. This work not only brings forward a strategy for tunable syngas production but also provides a new idea for the design of high-performance electrocatalysts.

## ASSOCIATED CONTENT

### Supporting Information

The Supporting Information is available free of charge at <https://pubs.acs.org/doi/10.1021/acs.chemmater.2c01917>.

TEM images, size distributions, SEM–EDS spectra, XPS spectra, PXRD patterns, chronoamperometry results, <sup>1</sup>H NMR and EIS spectra of Pd/Cu core/shell ico; TEM image, SEM–EDS spectrum, and HRTEM image of Pd<sub>2.2</sub>Cu ico after the durability test; and TEM images, PXRD patterns, and CO<sub>2</sub>RR performances of Pd ico and Pd/Cu core/shell nanocubes and tetrahedra (PDF)

## AUTHOR INFORMATION

### Corresponding Authors

**Nan Zhang** – Key Laboratory of Synthetic and Biological Colloids, Ministry of Education, School of Chemical and Material Engineering, International Joint Research Laboratory for Nano Energy Composites, Jiangnan University, Wuxi 214122, China; [orcid.org/0000-0002-2177-0544](https://orcid.org/0000-0002-2177-0544); Email: [nzhang@jiangnan.edu.cn](mailto:nzhang@jiangnan.edu.cn)

**Tianxi Liu** – Key Laboratory of Synthetic and Biological Colloids, Ministry of Education, School of Chemical and Material Engineering, International Joint Research Laboratory for Nano Energy Composites, Jiangnan University, Wuxi 214122, China; Email: [txliu@jiangnan.edu.cn](mailto:txliu@jiangnan.edu.cn)

### Authors

**Hanjun Li** – Key Laboratory of Synthetic and Biological Colloids, Ministry of Education, School of Chemical and Material Engineering, International Joint Research Laboratory for Nano Energy Composites, Jiangnan University, Wuxi 214122, China

**Shuxing Bai** – College of Chemistry and Chemical Engineering, Qingdao University, Qingdao 266071, China; [orcid.org/0000-0003-0767-2603](https://orcid.org/0000-0003-0767-2603)

**Longsheng Zhang** – Key Laboratory of Synthetic and Biological Colloids, Ministry of Education, School of Chemical and Material Engineering, International Joint Research Laboratory for Nano Energy Composites, Jiangnan University, Wuxi 214122, China

**Feili Lai** – Department of Chemistry, KU Leuven, Leuven 3001, Belgium; [orcid.org/0000-0002-4945-0737](https://orcid.org/0000-0002-4945-0737)

**Yao Chen** – Key Laboratory of Synthetic and Biological Colloids, Ministry of Education, School of Chemical and Material Engineering, International Joint Research Laboratory for Nano Energy Composites, Jiangnan University, Wuxi 214122, China

**Xiangmiao Zhu** – Key Laboratory of Synthetic and Biological Colloids, Ministry of Education, School of Chemical and Material Engineering, International Joint Research Laboratory for Nano Energy Composites, Jiangnan University, Wuxi 214122, China

Complete contact information is available at:

<https://pubs.acs.org/doi/10.1021/acs.chemmater.2c01917>

### Notes

The authors declare no competing financial interest.

## ACKNOWLEDGMENTS

This work was financially supported by the National Natural Science Foundation of China (NSFC) (grant no. 22105087) and Natural Science Foundation of Jiangsu Province (grant no. BK20210446). The authors thank the Central Laboratory, School of Chemical and Material Engineering, Jiangnan University.

## REFERENCES

- (1) Zhu, D. D.; Liu, J. L.; Qiao, S. Z. Recent Advances in Inorganic Heterogeneous Electrocatalysts for Reduction of Carbon Dioxide. *Adv. Mater.* **2016**, *28*, 3423–3452.
- (2) Han, N.; Ding, P.; He, L.; Li, Y.; Li, Y. Promises of Main Group Metal-Based Nanostructured Materials for Electrochemical CO<sub>2</sub> Reduction to Formate. *Adv. Energy Mater.* **2019**, *10*, 1902338.
- (3) Gu, Z.; Shen, H.; Chen, Z.; Yang, Y.; Yang, C.; Ji, Y.; Wang, Y.; Zhu, C.; Liu, J.; Li, J.; Sham, T. K.; Xu, X.; Zheng, G. Efficient Electrocatalytic CO<sub>2</sub> Reduction to C<sub>2+</sub> Alcohols at Defect-Site-Rich Cu Surface. *Joule* **2021**, *5*, 429–440.
- (4) Nitopi, S.; Bertheussen, E.; Scott, S. B.; Liu, X.; Engstfeld, A. K.; Horch, S.; Seger, B.; Stephens, I. E. L.; Chan, K.; Hahn, C.; Nørskov, J. K.; Jaramillo, T. F.; Chorkendorff, I. Progress and Perspectives of Electrochemical CO<sub>2</sub> Reduction on Copper in Aqueous Electrolyte. *Chem. Rev.* **2019**, *119*, 7610–7672.
- (5) Cheng, H.; Liu, S.; Zhang, J.; Zhou, T.; Zhang, N.; Zheng, X. S.; Chu, W.; Hu, Z.; Wu, C.; Xie, Y. Surface Nitrogen-Injection Engineering for High Formation Rate of CO<sub>2</sub> Reduction to Formate. *Nano Lett.* **2020**, *20*, 6097–6103.
- (6) Yin, P. F.; Fu, J.; Yun, Q.; Chen, B.; Liu, G.; Li, L.; Huang, Z.; Ge, Y.; Zhang, H. Preparation of Amorphous SnO<sub>2</sub>-Encapsulated Multi-phased Crystalline Cu Heterostructures for Highly Efficient CO<sub>2</sub> Reduction. *Adv. Mater.* **2022**, *34*, 2201114.
- (7) Han, N.; Sun, M.; Zhou, Y.; Xu, J.; Cheng, C.; Zhou, R.; Zhang, L.; Luo, J.; Huang, B.; Li, Y. Alloyed Palladium-Silver Nanowires Enabling Ultraprecise Carbon Dioxide Reduction to Formate. *Adv. Mater.* **2021**, *33*, 2005821.
- (8) Li, H.; Wen, P.; Itanze, D. S.; Hood, Z. D.; Ma, X.; Kim, M.; Adhikari, S.; Lu, C.; Dun, C.; Chi, M.; Qiu, Y.; Geyer, S. M. Colloidal Silver Diphosphide (AgP<sub>2</sub>) Nanocrystals as Low Overpotential Catalysts for CO<sub>2</sub> Reduction to Tunable Syngas. *Nat. Commun.* **2019**, *10*, 5724.
- (9) Peng, C.; Xu, Z.; Luo, G.; Yan, S.; Zhang, J.; Li, S.; Chen, Y.; Chang, L. Y.; Wang, Z.; Sham, T. K.; Zheng, G. Highly-Exposed Single-Interlayered Cu Edges Enable High-Rate CO<sub>2</sub>-to-CH<sub>4</sub> Electrosynthesis. *Adv. Energy Mater.* **2022**, *12*, 2200195.
- (10) Li, H.; Xiao, N.; Wang, Y.; Li, C.; Ye, X.; Guo, Z.; Pan, X.; Liu, C.; Bai, J.; Xiao, J.; Zhang, X.; Zhao, S.; Qiu, J. Nitrogen-Doped Tubular Carbon Foam Electrodes for Efficient Electroreduction of CO<sub>2</sub> to Syngas with Potential-Independent CO/H<sub>2</sub> Ratios. *J. Mater. Chem. A* **2019**, *7*, 18852–18860.
- (11) Shen, C.; Wang, P.; Li, L.; Huang, X.; Shao, Q. Phase and Structure Modulating of Bimetallic Cu/In Nanoparticles Realizes Efficient Electrosynthesis of Syngas with Wide CO/H<sub>2</sub> Ratios. *Nano Res.* **2021**, *15*, 528–534.
- (12) Lu, S.; Shi, Y.; Meng, N.; Lu, S.; Yu, Y.; Zhang, B. Electrosynthesis of Syngas via the Co-Reduction of CO<sub>2</sub> and H<sub>2</sub>O. *Cell Rep. Phys. Sci.* **2020**, *1*, 100237.
- (13) He, Q.; Liu, D.; Lee, J. H.; Liu, Y.; Xie, Z.; Hwang, S.; Kattel, S.; Song, L.; Chen, J. G. Electrochemical Conversion of CO<sub>2</sub> to Syngas with Controllable CO/H<sub>2</sub> Ratios over Co and Ni Single-Atom Catalysts. *Angew. Chem., Int. Ed.* **2020**, *59*, 3033–3037.
- (14) Hoffman, Z. B.; Gray, T. S.; Moraveck, K. B.; Gunnoe, T. B.; Zangari, G. Electrochemical Reduction of Carbon Dioxide to Syngas and Formate at Dendritic Copper-Indium Electrocatalysts. *ACS Catal.* **2017**, *7*, 5381–5390.
- (15) Huang, M.; Kong, X.; Wang, C.; Geng, Z.; Zeng, J.; Bao, J. Synthesis of Tunable Syngas on Cobalt-Based Catalysts towards Carbon Dioxide Reduction. *ChemNanoMat* **2020**, *7*, 2–6.
- (16) Daiyan, R.; Chen, R.; Kumar, P.; Bedford, N. M.; Qu, J.; Cairney, J. M.; Lu, X.; Amal, R. Tunable Syngas Production through CO<sub>2</sub> Electroreduction on Cobalt-Carbon Composite Electrocatalyst. *ACS Appl. Mater. Interfaces* **2020**, *12*, 9307–9315.
- (17) Xie, H.; Chen, S.; Ma, F.; Liang, J.; Miao, Z.; Wang, T.; Wang, H. L.; Huang, Y.; Li, Q. Boosting Tunable Syngas Formation via Electrochemical CO<sub>2</sub> Reduction on Cu/In<sub>2</sub>O<sub>3</sub> Core/Shell Nanoparticles. *ACS Appl. Mater. Interfaces* **2018**, *10*, 36996–37004.
- (18) Xu, J.; Li, X.; Liu, W.; Sun, Y.; Ju, Z.; Yao, T.; Wang, C.; Ju, H.; Zhu, J.; Wei, S.; Xie, Y. Carbon Dioxide Electroreduction into Syngas Boosted by a Partially Delocalized Charge in Molybdenum Sulfide Selenide Alloy Monolayers. *Angew. Chem., Int. Ed.* **2017**, *56*, 9121–9125.
- (19) Tackett, B. M.; Lee, J. H.; Chen, J. G. Electrochemical Conversion of CO<sub>2</sub> to Syngas with Palladium-Based Electrocatalysts. *Acc. Chem. Res.* **2020**, *53*, 1535–1544.
- (20) Xu, L.; Wang, X.; Ma, T.; Zhao, X. Seed-Mediated Growth of Au Core-Pd Shell-Structured Nanoparticles on a Polymer Nanofibrous Mat as a Highly Active Photocatalytic Composite Material. *Compos. Commun.* **2020**, *21*, 100406.
- (21) Ge, J.; Wei, P.; Wu, G.; Liu, Y.; Yuan, T.; Li, Z.; Qu, Y.; Wu, Y.; Li, H.; Zhuang, Z.; Hong, X.; Li, Y. Ultrathin Palladium Nanomesh for Electrocatalysis. *Angew. Chem., Int. Ed.* **2018**, *57*, 3435–3438.
- (22) Li, X.; Li, X.; Liu, C.; Huang, H.; Gao, P.; Ahmad, F.; Luo, L.; Ye, Y.; Geng, Z.; Wang, G.; Si, R.; Ma, C.; Yang, J.; Zeng, J. Atomic-Level Construction of Tensile-Strained PdFe Alloy Surface toward Highly Efficient Oxygen Reduction Electrocatalysis. *Nano Lett.* **2020**, *20*, 1403–1409.
- (23) Zhang, F. Y.; Sheng, T.; Tian, N.; Liu, L.; Xiao, C.; Lu, B. A.; Xu, B. B.; Zhou, Z. Y.; Sun, S. G. Cu Overlayers on Tetrahedral Pd Nanocrystals with High-Index Facets for CO<sub>2</sub> Electroreduction to Alcohols. *Chem. Commun.* **2017**, *53*, 8085–8088.
- (24) Lan, Y.; Niu, G.; Wang, F.; Cui, D.; Hu, Z. SnO<sub>2</sub>-Modified Two-Dimensional CuO for Enhanced Electrochemical Reduction of CO<sub>2</sub> to C<sub>2</sub>H<sub>4</sub>. *ACS Appl. Mater. Interfaces* **2020**, *12*, 36128–36136.
- (25) Zhang, W.; Qin, Q.; Dai, L.; Qin, R.; Zhao, X.; Chen, X.; Ou, D.; Chen, J.; Chuong, T. T.; Wu, B.; Zheng, N. Electrochemical Reduction of Carbon Dioxide to Methanol on Hierarchical Pd/SnO<sub>2</sub> Nanosheets with Abundant Pd-O-Sn Interfaces. *Angew. Chem., Int. Ed.* **2018**, *57*, 9475–9479.
- (26) Qin, B.; Li, Y.; Fu, H.; Wang, H.; Chen, S.; Liu, Z.; Peng, F. Electrochemical Reduction of CO<sub>2</sub> into Tunable Syngas Production by Regulating the Crystal Facets of Earth-Abundant Zn Catalyst. *ACS Appl. Mater. Interfaces* **2018**, *10*, 20530–20539.
- (27) Peng, W.; Jin, J.; Yang, S.; Shen, Z.; Wang, H.; Zhang, J.; Li, G. Hollow Co<sub>9</sub>S<sub>8</sub> Spheres-Derived Polyhedrons Uniformly Anchored on N, S-doped Graphene for Efficient Oxygen Electrocatalysts. *Compos. Commun.* **2021**, *23*, 100587.
- (28) Guo, S.; Zhao, S.; Wu, X.; Li, H.; Zhou, Y.; Zhu, C.; Yang, N.; Jiang, X.; Gao, J.; Bai, L.; Liu, Y.; Lifshitz, Y.; Lee, S. T.; Kang, Z. A Co<sub>3</sub>O<sub>4</sub>-CDots-C<sub>3</sub>N<sub>4</sub> Three Component Electrocatalyst Design Concept for Efficient and Tunable CO<sub>2</sub> Reduction to Syngas. *Nat. Commun.* **2017**, *8*, 1828.
- (29) Tao, L.; Sun, M.; Zhou, Y.; Luo, M.; Lv, F.; Li, M.; Zhang, Q.; Gu, L.; Huang, B.; Guo, S. A General Synthetic Method for High-Entropy Alloy Subnanometer Ribbons. *J. Am. Chem. Soc.* **2022**, *144*, 10582–10590.
- (30) Huang, H.; Jia, H.; Liu, Z.; Gao, P.; Zhao, J.; Luo, Z.; Yang, J.; Zeng, J. Understanding of Strain Effects in the Electrochemical Reduction of CO<sub>2</sub>: Using Pd Nanostructures as an Ideal Platform. *Angew. Chem., Int. Ed.* **2017**, *56*, 3594–3598.
- (31) Luo, M.; Guo, S. Strain-Controlled Electrocatalysis on Multimetallic Nanomaterials. *Nat. Rev. Mater.* **2017**, *2*, 17059.
- (32) Wang, H.; Jiao, L.; Zheng, L.; Fang, Q.; Qin, Y.; Luo, X.; Wei, X.; Hu, L.; Gu, W.; Wen, J.; Zhu, C. PdBi Single-Atom Alloy Aerogels for Efficient Ethanol Oxidation. *Adv. Funct. Mater.* **2021**, *31*, 2103465.
- (33) Zhang, S.; Liu, K.; Liu, Z.; Liu, M.; Zhang, Z.; Qiao, Z.; Ming, L.; Gao, C. Highly Strained Au-Ag-Pd Alloy Nanowires for Boosted Electrooxidation of Biomass-Derived Alcohols. *Nano Lett.* **2021**, *21*, 1074–1082.
- (34) Wang, Z.; Chen, L.; Xu, S.; Zhang, D.; Zhou, X.; Wu, X.; Xie, X.; Qiu, X. Cobalt Vanadium Layered Double Hydroxide/FeOOH Heterostructure Catalyst with Strong Electron Interactions for Stable Oxygen Evolution Performance. *Compos. Commun.* **2021**, *27*, 100780.
- (35) Yang, D.; Zhu, Q.; Sun, X.; Chen, C.; Guo, W.; Yang, G.; Han, B. Electrosynthesis of a Defective Indium Selenide with 3D Structure on a

Substrate for Tunable CO<sub>2</sub> Electroreduction to Syngas. *Angew. Chem., Int. Ed.* **2020**, *59*, 2354–2359.

(36) Ross, M. B.; Dinh, C. T.; Li, Y.; Kim, D.; De Luna, P.; Sargent, E. H.; Yang, P. Tunable Cu Enrichment Enables Designer Syngas Electrosynthesis from CO<sub>2</sub>. *J. Am. Chem. Soc.* **2017**, *139*, 9359–9363.

(37) Zhang, J.; Yin, R.; Shao, Q.; Zhu, T.; Huang, X. Oxygen Vacancies in Amorphous InO<sub>x</sub> Nanoribbons Enhance CO<sub>2</sub> Adsorption and Activation for CO<sub>2</sub> Electroreduction. *Angew. Chem., Int. Ed.* **2019**, *58*, 5609–5613.

## Recommended by ACS

### Methanol Synthesis Over PdIn, In<sub>2</sub>O<sub>3</sub>, and CuZn From First-Principles Microkinetics: Similarities and Differences

Minttu Kauppinen, Henrik Grönbeck, *et al.*

SEPTEMBER 01, 2022  
THE JOURNAL OF PHYSICAL CHEMISTRY C

READ 

### Atomically Reconstructed Palladium Metallene by Intercalation-Induced Lattice Expansion and Amorphization for Highly Efficient Electrocatalysis

Minghao Xie, Guihua Yu, *et al.*

AUGUST 10, 2022  
ACS NANO

READ 

### CO<sub>2</sub> Electroreduction on Unsupported PdPt Aerogels: Effects of Alloying and Surface Composition on Product Selectivity

Justus S. Diercks, Thomas J. Schmidt, *et al.*

JULY 06, 2022  
ACS APPLIED ENERGY MATERIALS

READ 

### Interplay between Surface-Adsorbed CO and Bulk Pd Hydride under CO<sub>2</sub>-Electroreduction Conditions

Justus S. Diercks, Thomas J. Schmidt, *et al.*

AUGUST 17, 2022  
ACS CATALYSIS

READ 

Get More Suggestions >